Polyelectrolyte/surfactant films: from 2D to 3D structural control

Javier Carrascosa-Tejedor[1,2], Andreas Santamaria[1,3], Andrea Tummino[1], Imre Varga[4], Marina Efstratiou[2], M. Jayne Lawrence[2], Armando Maestro[5,6*] and Richard A. Campbell[2*]

1. Institut Laue-Langevin, 71 avenue des Martyrs, CS20156, 38042 Grenoble Cedex 9, France
2. Division of Pharmacy and Optometry, Faculty of Biology, Medicine and Health, University of Manchester, Oxford Road, Manchester M13 9PT, United Kingdom
3. Departamento de Química Física, Facultad de Ciencias, Universidad Complutense de Madrid, Ciudad Universitaria s/n, 28040 Madrid, Spain
4. Institute of Chemistry, Eötvös Loránd University, 112, P.O. Box 32, Budapest H-1518, Hungary
5. Centro de Física de Materiales (CSIC, UPV/EHU) - Materials Physics Center MPC, Paseo Manuel de Lardizabal 5, E-20018 San Sebastián, Spain
6. IKERBASQUE—Basque Foundation for Science, Plaza Euskadi 5, Bilbao, 48009 Spain

** corresponding authors: armando.maestro@ehu.eus & richard.campbell@manchester.ac.uk*

Electronic Supporting Information

The Electronic Supporting Information contains: (1) zeta potential measurements of PLL/SDS aggregates, (2) materials and methods, (3) low-Q_z compositional analysis: fitting, (4) ellipsometry data on PLL/SDS spread film dynamics, (5) BAM images, (6) full-Q_z structural analysis: fitting and parameters, and (7) mid-Q_z structural dynamics analysis: fitting.

1 Zeta potential measurements of PLL/SDS aggregates

100 ppm PLL mixed with an SDS concentration varying from 0.4 mM to 1 mM results in a transition from positively to negatively charged PLL/SDS aggregates. Figure SI1 shows the variation of the ζ-potential of PLL/SDS aggregates with respect to the SDS concentration. While stoichiometric charge mixing of the components would require 0.48 mM SDS, excess surfactant is needed to produce neutral aggregates: 0.63 mM in total. Since the excess of SDS needed for the neutralization of aggregates is low, a high binding efficiency of SDS to PLL chains is evident.

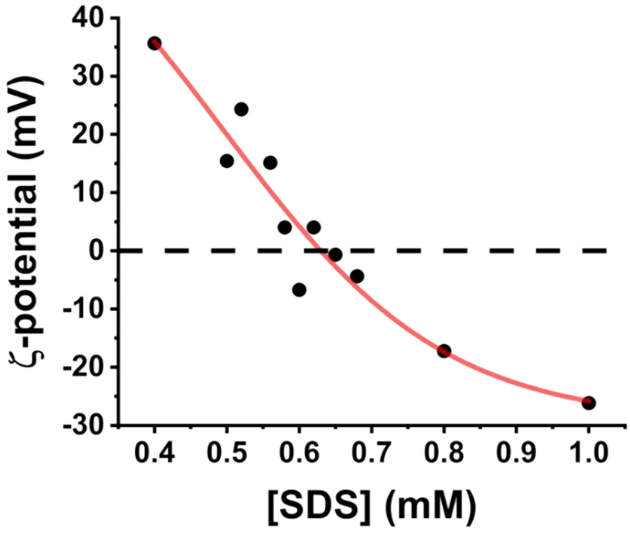

Figure SI1. Variation of the ζ-potential of freshly prepared PLL/SDS mixtures at a constant concentration of 100 ppm PLL varying the concentration of SDS between 0.4–1.0 mM. Experimental data points are shown (black circles) together with a sigmoidal fit (red line). The black dashed line indicates neutral charge.

2 Materials and methods

2.1 Materials

15–30 kDa poly-(L-lysine) (PLL) hydrobromide powder, poly(sodium styrenesulfonate) (NaPSS), sodium dodecyl sulfate (SDS), sodium dodecyl-d25 sulfate (d-SDS), dodecyltrimethylammonium bromide (DTAB), acetone (≥99.5%), ethanol (≥99.8%) and D_2O were purchased from Sigma

Aldrich. PLL, NaPSS and D_2O were used as received. SDS and DTAB were recrystallized twice in ethanol and 4:1 acetone:ethanol mixtures, respectively, followed by drying under vacuum. Ultra-pure water was generated by passing deionized water through a Milli-Q unit (total organic content ≤ 4 ppb, resistivity = 18 MΩ·cm).

2.2 Sample preparation

PLL/SDS mixtures were prepared pouring an aliquot of PLL 200 ppm solution into a clean vessel containing a magnetic stirrer. An aliquot of the same volume of SDS 1.6 mM was then rapidly added to the vessel with stirring maintained for 3–5 s. PLL/SDS mixtures were always prepared immediately before use (maximum of 1 min) to limit the growth of any aggregates prior to the experiment. NaPSS/DTAB mixtures were prepared by pouring solutions of PSS 200 ppm and DTAB 20 mM at the same time into the vessel.

2.3 Zeta potential

A Zetasizer Nano ZS90 (Malvern Instruments Ltd., U.K.) using laser doppler velocimetry and phase analysis light scattering techniques (M3-PALS) was used in this work to determine the ζ-potential of PLL/SDS freshly prepared solutions. Measurements were performed with a constant concentration of PLL 100 ppm by varying the SDS concentration between 0.4 – 1.0 mM.

2.4 Langmuir trough

The Langmuir trough technique has been used to study the behaviour of PLL/SDS spread films during consecutive compression/expansion cycles by using two movable barriers. The surface pressure, Π, which is the difference between the surface tension of pure water and that of the film, was recorded using a Wilhelmy plate. In the present work, we have used this technique to characterize the dynamic behaviour of the films during compression/expansion cycles, as well as the stability of the extended structures over time at a constant area. The Langmuir trough has also been coupled to different reflectometry techniques.

In the present work, three different Langmuir troughs were used, namely a Kibron G1 (Finland) with dimensions of 260 × 80 mm (this trough was coupled to the Brewster angle microscope and

the Beaglehole ellipsometer, using a maximum and minimum surface area of 166 and 88 cm^2, respectively; the speed of the barriers during the compression/expansion cycles was 3.16 cm^2/min, i.e., 49 min/cycle); a Kibron G2 (Finland) with dimensions of 405 × 80 mm (this trough was coupled to the Accurion ellipsometer, using a maximum and minimum surface area of 280 and 140 cm^2, respectively; the speed of the barriers during the compression/expansion cycles was 5.4 cm^2/min, i.e., 49 min/cycle); and a Nima (UK) with dimensions of 300 × 100 mm (this trough was coupled to the neutron reflectometer, using a maximum and minimum surface area of 265 and 130 cm^2, respectively; the speed of the barriers during the compression/expansion cycles was 5.5 cm^2/min, i.e., 49 min/cycle). The trough and barriers were carefully cleaned with detergent, ethanol and water before filling them with Milli-Q water. Subsequently, a freshly prepared solution of PLL/SDS aggregates was spread dropwise across the entire air/water interface (1130, 1900 and 1800 µL for the respective three troughs mentioned above). 530 µL of PSS/DTAB aggregates were spread in the experiment performed using the Kibron G2 trough. After 20 min of equilibration, the variation of the surface pressure as a function of the area was recorded.

2.5 Ellipsometry

Ellipsometry is a non-destructive optical technique based on determination of changes in the polarization of light upon reflection at an interface. From these polarization changes, it is possible to obtain information about the phase difference between the parallel and perpendicular components of the incident and the reflected beam, Δ, and the ratio of amplitudes of the parallel and perpendicular components defined as $\tan\Psi = |r_p|/|r_s|$. The ellipsometric angles are related to the total reflection coefficients by the ellipticity, ρ, defined as $\rho = r_p/r_s = \tan\Psi^{i\Delta}$, that depends on the angle of incidence, the wavelength and both the thickness and the dielectric properties of the material. At the air/water interface, Δ is much more sensitive than Ψ to changes in coverage of thin films.[1,2] Often only changes in Δ are analysed, which is the approach taken in the present work, where $d\Delta = \Delta_{P/S}$ (for the P/S film) – Δ_{water} (for pure water). Values of $d\Delta$ are presented to remove the contribution of surface roughness leading to the response of $d\Delta$ being sensitive to

the surface excess of fluid thin films, and temporal fluctuations being related to lateral heterogeneity on the micrometer length scale.[3]

Ellipsometry experiments were performed using two different ellipsometers. An Accurion EP4 ellipsometer (Germany) equipped with a blue diode laser with a wavelength of λ = 489.2 nm was used to record the stability measurements presented in Figure 1A at an angle of incidence of 50° and a data acquisition rate of 0.1 Hz. A Beaglehole Picometer Light ellipsometer (New Zealand) equipped with a He-Ne laser with a wavelength of λ = 632.8 nm was used to record the dynamics presented in Figure S3 at an angle of incidence of 51° and a data acquisition rate of 0.2 Hz.

2.6 Brewster angle microscopy

Brewster angle microscopy is an optical technique that allows characterizing the homogeneity/inhomogeneity of the film as well as the interfacial organization of the material on the micrometer scale.[4] An Accurion Nanofilm EP3 Brewster angle microscope (Germany) equipped with a Nd:YAG laser (λ = 532 nm) was used. Images of the PLL/SDS film at the air/water interface were taken at an angle of incidence equal to the Brewster angle, 53.1° for the air/water interface, without background subtraction and using a 10× objective and a CCD detector. The polarizer and analyzer were adjusted so that p-polarized light was reflected at the interface. Thus, the air/water interface appears as a black image, the presence of a homogeneous fluid film with a different refractive index appears as a gray image and the additional layer of extended structures appears as brighter regions.

2.7 Neutron reflectometry

Neutron reflectometry (NR) has been used as a powerful tool to elucidate the structure and dynamic behaviour of a wide variety of systems at interfaces.[5–7] Specular reflectivity, R, defined as the number of neutrons scattered from the interface divided by that in the incident beam, is recorded at grazing incident angles as a function of the momentum transfer normal to the interface, Q_z, defined as:

$$Q_z = \frac{4\pi sin\theta}{\lambda} \quad (1)$$

where λ is the wavelength and θ the incident angle. Neutron scattering from a molecule depends on its scattering length density (SLD), ρ, which is defined as the ratio of the sum of the coherent scattering lengths, b, of its constituent atoms and its molecular volume, V_m. The use of isotopic contrast variation allows one to resolve the structure and composition of the interface by the substitution of hydrogen for deuterium, which maximizes the differences between the molecules present at the interface and/or the subphase. Indeed, a mixture of 8.1% v/v D_2O in H_2O presents particular interest because its SLD, like that of air, is zero, which is why it is known as air contrast matched water (ACMW), making the subphase practically invisible to neutrons.

Neutron reflectivity measurements were performed on the time-of-flight neutron reflectometer FIGARO at the Institut Laue-Langevin (Grenoble, France).[8] A chopper pair was used to generate neutron pulses with a wavelength resolution of 7% dλ/λ. Three different incident angles θ = 0.63°, 1.97° and 3.78° were used to record the low-Q_z, mid-Q_z and high-Q_z range, respectively. The data were reduced using COSMOS[9] and analyzed with Motofit.[10] The three different implementations of NR used in this work are explained in detail in sections 3, 6 and 7.

3 Low-Q_z compositional analysis: fitting

The use of FIGARO with its low natural incident angle allows a high-flux configuration at a stable reactor source that makes it a unique instrument to study dynamics at the air/water interface.[5,8]

The recently developed low-Q_z analysis was used to follow the variations of the surface excess of PLL and SDS during the compression/expansion of the film.[11] The NR data were reduced over 4.5–12 Å to get Q_z = 0.01–0.03 $Å^{-1}$ where the reflectivity profile is insensitive to the structure of the film but very sensitive to the surface excess, which for a single component is defined as:

$$\Gamma = \frac{\rho d}{bN_A} \quad (2)$$

where d is the thickness of the layer and N_A is Avogadro's number. Background was not subtracted from the data and two isotopic contrasts were used: (1) PLL with d-SDS in ACMW and (2) PLL with SDS in ACMW. Then, two different data sets can be used to resolve Γ_{PLL} and Γ_{SDS} by solving the linear equations:

$$\rho_d \cdot d_d = N_A \cdot (\Gamma_{PLL} \cdot b_{PLL} + \Gamma_{SDS} \cdot b_{d-SDS}); \quad (3)$$

$$\rho_h \cdot d_h = N_A \cdot (\Gamma_{PLL} \cdot b_{PLL} + \Gamma_{SDS} \cdot b_{h-SDS}); \quad (4)$$

where ρ_d = 1 × 10^{-6} Å^{-2} and ρ_h = 4 × 10^{-6} Å^{-2} are the values of SLD fixed for contrast 1 and 2, respectively, d_d and d_h are the thickness values fitted for contrast 1 and 2, respectively. While the strong scattering in contrast 1 allows resolving Γ_{SDS} in 1 min slices, the low scattering in contrast 2 makes it is necessary to accurately determine the background and resolve 3 min slices in order to have better statistics, less noisy data and resolve accurately Γ_{PLL}. For that reason, the background was determined as the average value from a series of measurements of the air/ACMW interface using 1 min slices (3.74 × 10^{-5}) and 3 min slices (3.76 × 10^{-5}). The parameters d_d and d_h were fitted using the fit batch data option of Motofit,[10] a single layer model and a roughness of 3.5 Å and the results were then used to solve equations 3 and 4. Table SI1 shows the values of scattering length, molecular volume and scattering length density used for each component studied in this work.

Table SI1. Scattering length (b), molecular volume (V_m) and scattering length density (ρ) used in this work for the different components studied.

Component	b (fm)	V_m (Å^3)	ρ (x 10^{-6} Å^{-2})
SS Headgroups	29.71	61	4.87
$C_{12}H_{25}$-Chains	–13.76	352	–0.39
$C_{12}D_{25}$-Chains	246.53	352	7.00
SDS Molecules	15.95	413	0.39
d_{25}-SDS Molecules	276.24	413	6.69
PLL (in ACMW)	18.85	173	1.09
PLL (in D_2O)	53.35	173	3.09

4 Ellipsometry data on PLL/SDS spread film dynamics

In order to verify if the surface pressure dynamics and the variation of interfacial material in the film is reproducible, 6 consecutive compression/expansion cycles of a PLL/SDS film were performed. In addition to the data shown in Figure 1C, where Γ_{SDS} and Γ_{PLL} are reproducible over three cycles, Figure SI2 shows that the response of the film in terms of Π and $d\Delta$ is very similar over 6 consecutive cycles. These results indicate that the material expelled from the monolayer to extended structures in each compression is efficiently reincorporated during each expansion, proving the high reproducibility of PLL/SDS spread film dynamics.

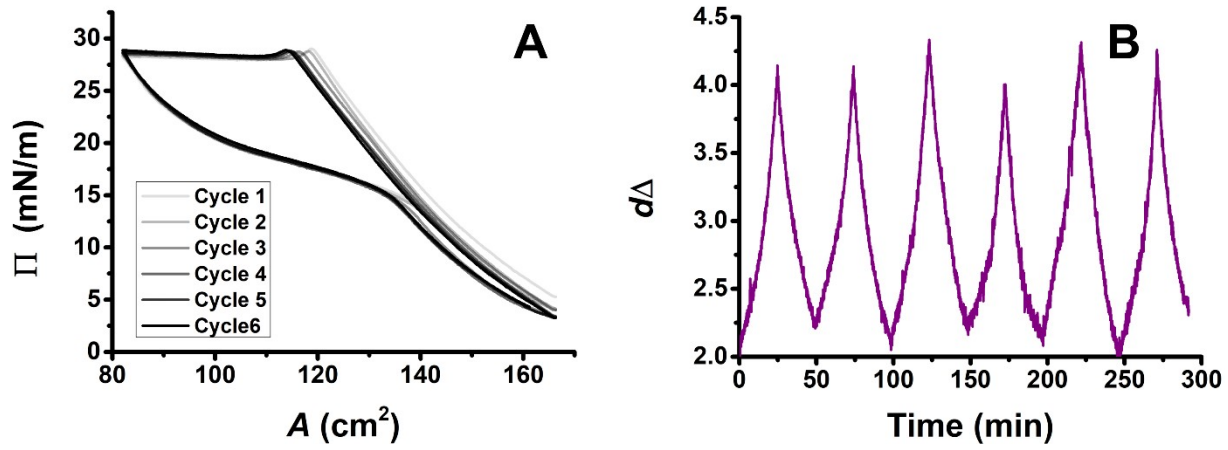

Figure SI2. Variation of (A) Π as a function of surface area and (B) $d\Delta$ as a function of time during 6 consecutive compression/expansion cycles for PLL/SDS spread films.

5 BAM images

The BAM images shown in Figure 1D are reproduced in Figure SI3 at higher image resolution. Before collapse, it is possible to observe the presence of a homogeneous film with a refractive index different to that of water, the intensity of which increases with the compression. After the collapse, the presence of extended structures below the surface monolayer causes another refractive index change such that discrete regions start to become visible on the µm-scale.

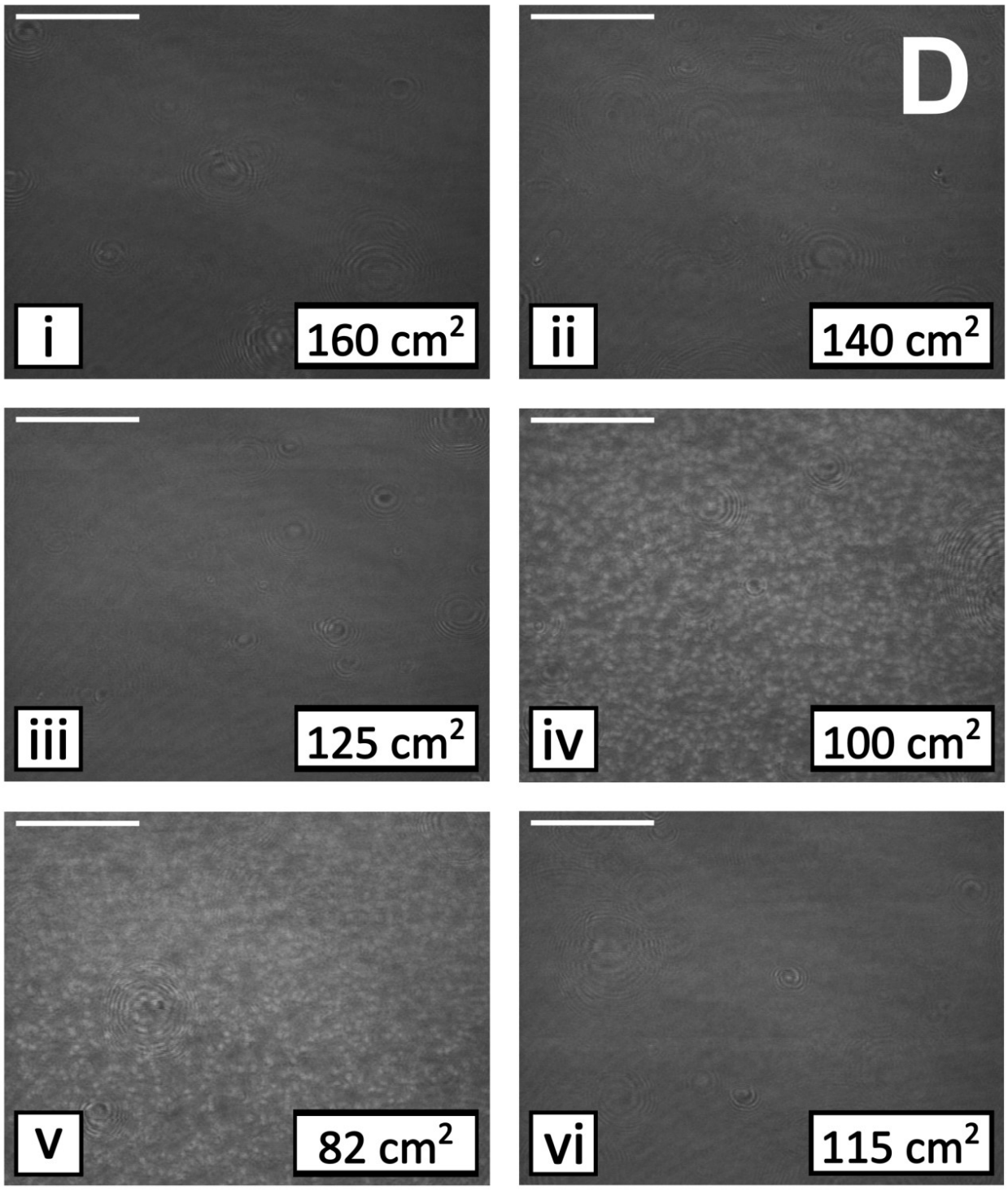

Figure SI3. BAM images of PLL/SDS films at different compression states. The states i-vi correspond to the states indicated in Figure 1B.

Quantitative analysis of the BAM image in the maximum compression state v has been carried out (Figure SI4). ImageJ software was used to clean the image and calculate the coverage (i.e. area) occupied by the extended structures. Although calculation of the coverage varied according to the threshold used for the analysis, the value obtained was ~ 30%. The analysis has shown generally that coverage of the extended structures formed after the collapse increases with compression, which is in keeping with the result from the mid-Q_z analysis in Figure 3.

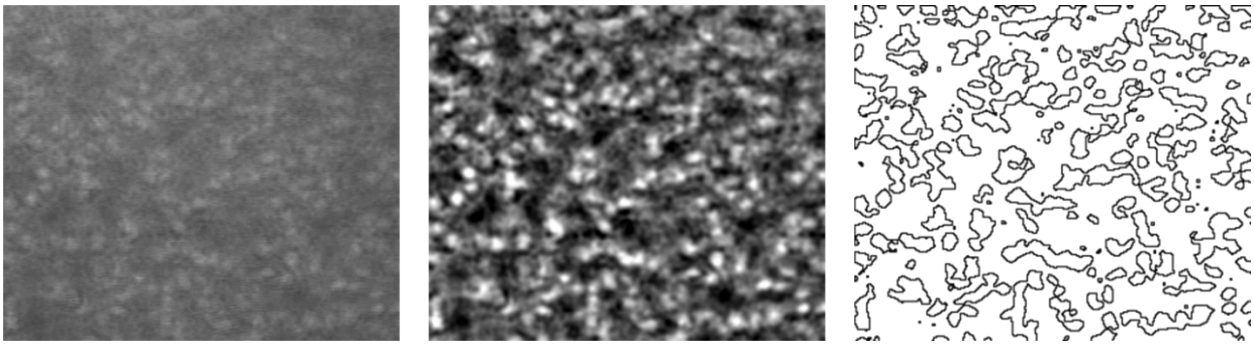

Figure SI4. Zoom of a region of the BAM image in the compression state v (left) together with image cleaning treatment (centre) and calculation of the coverage occupied by the extended structures (right).

6 Full-Q_z structural analysis: fitting and parameters

The full-Q_z range Q_z = 0.01–0.25 Å^{-1} was recorded to resolve the structure of PLL/SDS films at high compression ratio in 4 isotopic contrasts: PLL with d-SDS in ACMW, PLL with d-SDS in D_2O, PLL with h-SDS in D_2O and PLL with h-SDS in ACMW. The background was subtracted from the data using the area detector.

The global fit of the full-Q_z data has been performed considering a model comprising four stratified layers as it was the smallest number of layers to result in a satisfactory fit of the data: 1) surfactant tails, 2) surfactant headgroups with PLL electrostatically bound and solvent, 3) PLL layer and solvent, and 4) the extended structures formed by the surfactant molecules expelled from the interface and solvent. Each layer, i, is characterized by four parameters: the SLD (ρ_i), the thickness (d_i), the roughness and the solvent volume fraction ($v_{f,i}$). Firstly, a roughness of 3.5 Å

consistent with the presence of capillary waves was applied to all interfaces.[12] Secondly, we considered that the SDS monolayer (i.e. the surfactant layer in contact with air with hydrated polyelectrolyte bound to the headgroups) surface excess is equal to 4.0 ± 0.1 μmol/m^2 as obtained from the low-Q_z analysis when the film collapses. Thus, the thickness of the surfactant tails layer was fixed to 8.5 Å. In addition, the surface excess of surfactant tails must be equal to the surface excess of headgroups to ensure physical reality. Besides, here the interfacial film is composed of surfactant and polyelectrolyte that interact electrostatically, making the headgroups layer more condensed due to the presence of PLL. Since PLL present labile protons in the amine groups that can exchange with the solution, we have considered a 90% of proton/deuterium exchange as generally considered for proteins. Therefore, another constraint is introduced as the SLD of the headgroups layer must be consistent between the contrasts in ACMW, where the SLD of PLL is equal to 1.09×10^{-6} Å^{-2}, and the contrast in D_2O, where the SLD of PLL is equal to 3.09×10^{-6} Å^{-2}. Finally, the parameters that have been fitted are d and v_f of layers 3 (PLL) and 4 (extended structures). The amount of PLL in the headgroups has been fixed but iteratively modified until the difference between the model and the experimental data (χ^2) is minimized, thus obtaining the model that best represents the structure of the P/S film. Residual background values were used as follows: 1×10^{-7} for d-SDS in ACMW, 3×10^{-7} for d-SDS and h-SDS in D_2O, and 4×10^{-6} for h-SDS in ACMW. Table SI2 shows the parameters used and fitted in the full-Q_z structural analysis. The uncertainties of the fitting parameters have been calculated as the difference between the optimised parameter and the variation of the optimised parameter that gives rise to an increase of the χ^2 of the fit by 10%. Finally, the uncertainties of the surface excess values of SDS and PLL derived from the full-Q_z fit can be determined from the uncertainties in layer 2 and 3 for PLL, and layers 1, 2 and 4 for SDS. Thus, the uncertainties of the surface excess has been calculated as the square-root of the linear sum of squared standard uncertainties.

Table SI2. Thickness (d_i), scattering length density (ρ_i), solvent volume fraction (v_{fi}) and composition obtained from the correspondent fit for each layer of the PLL/SDS films spread from overcharged aggregates, where *i* is the layer number. The parameters fitted are d_3, V_{f3}, d_4 and V_{f4}.

Layer	Parameter	d-SDS/ACMW	d-SDS/D_2O	h-SDS/D_2O	h-SDS/ACMW
1	d_1 (Å)	8.5 ± 0.2	8.5 ± 0.2	8.5 ± 0.2	8.5 ± 0.2
	ρ_1 (x 10^{-6} Å^{-2})	7	7	-0.39	-0.39
	v_{f1}	0	0	0	0
	Composition	100% SDS chains	100% SDS chains	100% SDS chains	100% SDS chains
2	d_2 (Å)	4	4	4	4
	ρ_2 (x 10^{-6} Å^{-2})	2.90	3.94	3.94	2.90
	v_{f2}	23 ± 1	23 ± 1	23 ± 1	23 ± 1
	Composition	37% SDS heads 40% PLL 23% solvent	37% SDS heads 40% PLL 23% solvent	37% SDS heads 40% PLL 23% solvent	37% SDS heads 40% PLL 23% solvent
3	d_3 (Å)	9.6 ± 0.7	9.6 ± 0.7	9.6 ± 0.7	9.6 ± 0.7
	ρ_3 (x 10^{-6} Å^{-2})	1.09	3.09	3.09	1.09
	v_{f3}	48 ± 4	48 ± 4	48 ± 4	48 ± 4
	Composition	52% PLL 48% solvent	52% PLL 48% solvent	52% PLL 48% solvent	52% PLL 48% solvent
4	d_4 (Å)	21.8 ± 0.8	21.8 ± 0.8	21.8 ± 0.8	21.8 ± 0.8
	ρ_4 (x 10^{-6} Å^{-2})	6.69	6.69	0.39	0.39
	v_{f4}	81.2 ± 0.7	81.2 ± 0.7	81.2 ± 0.7	81.2 ± 0.7
	Composition	19% SDS 81% solvent	19% SDS 81% solvent	19% SDS 81% solvent	19% SDS 81% solvent

The surface excess of SDS obtained from the full-Q_z fit (5.7 ± 0.3 µmol/cm^2) is in agreement with the one obtained from the low-Q_z at maximum compression (5.6 ± 0.1 µmol/cm^2). However, a significant lower surface excess of PLL is obtained from the low-Q_z (4.7 ± 0.3 µmol/cm^2) respect to the full-Q_z (6.3 ± 0.5 µmol/cm^2), which could be related to the fact that the low-Q_z present high sensitivity to the surface excess but not to the interfacial structure, while the full-Q_z is very sensitive to the structure but less to the surface excess. Indeed, the variation of the thickness and the solvent content of the PLL layer provides fits with similar χ^2 but a surface excess varying from 5.8 ± 0.5 to 6.7 ± 0.7 µmol/cm^2 (green square and circle in Table SI3 and Figure SI5. respectively), showing that the sensitivity to the surface excess of this layer in the full-Q_z is lower. Table SI3 and Figure SI5 shows the results obtained from the fits varying the thickness and the solvent of the PLL layer.

Table SI3. χ^2 and Γ_{PLL} values of different fits varying the amount of solvent of the PLL layer. The first three columns show the results of the fits fixing the thickness of the film and varying the amount of solvent. The last three columns show the results of the fits changing the solvent and fitting the thickness of the PLL layer. The green box indicates the fits with similar and low χ^2 values shown in Figure SI5 with a green circle.

$d_{4,fixed}$ = 9.6 Å			$d_{4,fitted}$		
$v_{f,4}$ (%)	χ^2	Γ_{PLL}	d (Å)	χ^2	Γ_{PLL}
20	31.7741	8.99	7.00	12.8575	6.91
25	23.2029	8.52	7.41	10.8608	6.87
30	16.2872	8.05	7.85	9.00087	6.81
35	11.0186	7.59	8.32	7.35884	6.73
40	7.39466	7.12	8.82	6.04526	6.62
45	5.41828	6.66	9.35	5.21099	6.47
50	5.09806	6.19	9.91	5.06135	6.29
55	6.44817	5.73	10.47	5.87218	6.06
60	9.48864	5.26	10.99	8.0018	5.76
65	14.2441	4.80	11.41	11.8823	5.37
70	20.7463	4.33	11.65	17.9588	4.89

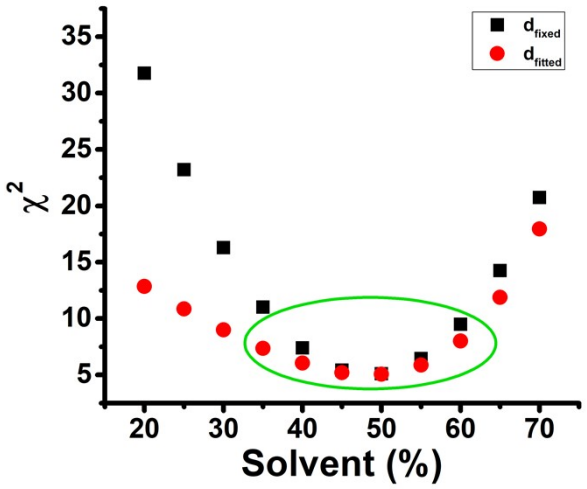

Figure SI5. Variation of χ^2 of different fits varying the amount of solvent in the PLL layer and fixing (black squares) or fitting (red circles) its thickness. The green circle indicates the region where the amount of solvent can vary from 35% to 60% yielding fits with similar χ^2.

7 Mid-Q_z structural dynamics analysis: fitting

A novel time-resolved method was used to follow variations of the reflectivity in the mid-Q_z range allowing the characterization of structural changes during film dynamics. Data were recorded using an incident angle of 1.97° and reduced over 3.6–20 Å to get Q_z = 0.02–0.12 Å^{-1}. The reason why we chose the mid-Q_z region to follow the structural dynamics is because the Keissig fringe that reveals the presence of the extended structures appears in this region. In addition, the peak of the neutron flux is at Q_z = 0.1 Å^{-1} where the Keissig fringe appears. We chose the contrast of PLL with h-SDS in D_2O because it is very sensitive to the presence of the surfactant extended structure as the difference in scattering between the surfactant chains and the solvent is very high, while it is less sensitive to the monolayer as the difference in scattering between air and surfactant chains is low. Thus, the formation of an extended structure of hydrogenous material in D_2O and the incident angle used offer the optimal conditions to follow the structural changes taking place during the collapse of the film.

We have fitted the mid-Q_z data with two different approaches showing that the decrease in reflectivity when we compress beyond the collapse of the film is due to the increase in the coverage of the extended structures and not its thickness. In both cases the model that best fits the full-Q_z data reported in Table SI2 has been used, varying only the coverage and/or thickness of the fourth layer. The first approach consists of a batch fit of the coverage fixing the thickness to the one obtained in the full-Q_z model (d_4 = 21.8 Å). The second approach consists of a batch data fit of the coverage fixing the thickness to d_4 = 21.8 × (Cov./Cov.max) Å, where Cov. is the coverage obtained in the previous fit and Cov._{max} is the one obtained at full compression, i.e., 16%. In this way, we can keep constant the volume fraction and verify if the changes in reflectivity results from changes in the coverage (approach 1) or thickness (approach 2) looking at the χ^2 obtained in each case. Table SI4 shows the values of coverage and χ^2 derived from the fits and Figure SI6 shows the comparison between the χ^2 values obtained for each slice using both approaches. The 17- and 22-min slices correspond to the first and the last slice recorded in the Π plateau region, respectively. The results show that a lower χ^2 is obtained for all slices using the approach 1, with a maximum difference of 30% in the slice 19. Therefore, we demonstrate that

the structural changes taking place during the collapse of the film are due to an increase of the coverage and not the thickness.

Table SI4. Values of coverage and χ^2 obtained from the fits of 1-min slices in the Π plateau region using approaches 1 and 2 described in the text.

	Approach 1 d_4 = 22 Å			Approach 2 $d_4 = 22 \cdot (\text{Cov.}/\text{Cov.}_{max})$ Å		
Slice (min)	**d_4 (Å)**	**Coverage (%)**	**χ^2**	**d_4 (Å)**	**Coverage (%)**	**χ^2**
17	22	3	1.316	4	24	1.463
18	22	6	2.126	9	19	2.880
19	22	8	2.318	11	18	3.263
20	22	11	1.533	15	17	2.153
21	22	14	1.427	19	17	1.788
22	22	16	1.830	22	--	--

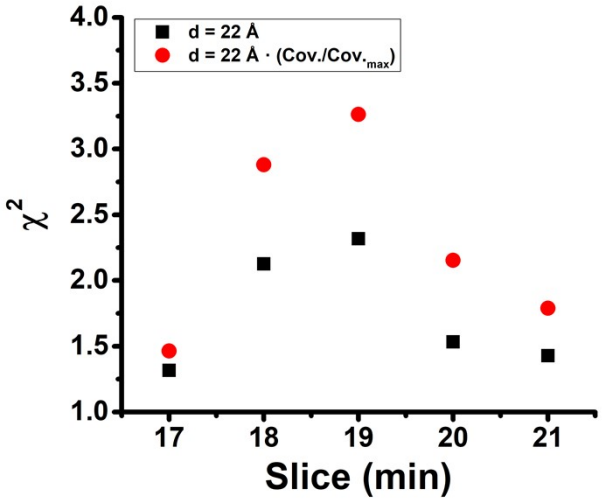

Figure SI6 Variation of χ^2 for the fitting of each 1-min slice of the mid-Q_z data from NR of PLL/SDS spread films in the Π plateau region using approaches 1 (black squares) and 2 (red circles) described in the text.

References

(1) De Feijter, J. A.; Benjamins, J.; Veer, F. A. Ellipsometry as a Tool to Study the Adsorption Behavior of Synthetic and Biopolymers at the Air-Water Interface. *Biopolymers* **1978**, *17*, 1759–1772. https://doi.org/10.1002/BIP.1978.360170711.

(2) Clifton, L. A.; Campbell, R. A.; Sebastiani, F.; Campos-Terán, J.; Gonzalez-Martinez, J. F.; Björklund, S.; Sotres, J.; Cárdenas, M. Design and Use of Model Membranes to Study Biomolecular Interactions Using Complementary Surface-Sensitive Techniques. *Adv. Colloid Interface Sci.* **2020**, *277*, 102118. https://doi.org/10.1016/j.cis.2020.102118.

(3) Tonigold, K.; Varga, I.; Nylander, T.; Campbell, R. A. Effects of Aggregates on Mixed Adsorption Layers of Poly(Ethylene Imine) and Sodium Dodecyl Sulfate at the Air/Liquid Interface. *Langmuir* **2009**, *25* (7), 4036–4046. https://doi.org/10.1021/la8028325.

(4) Daear, W.; Mahadeo, M.; Prenner, E. J. Applications of Brewster Angle Microscopy from Biological Materials to Biological Systems. *Biochim. Biophys. Acta - Biomembr.* **2017**, *1859* (10), 1749–1766. https://doi.org/10.1016/j.bbamem.2017.06.016.

(5) Campbell, R. A. Recent Advances in Resolving Kinetic and Dynamic Processes at the Air/Water Interface Using Specular Neutron Reflectometry. *Curr. Opin. Colloid Interface Sci.* **2018**, *37*, 49–60. https://doi.org/10.1016/j.cocis.2018.06.002.

(6) Braun, L.; Uhlig, M.; von Klitzing, R.; Campbell, R. A. Polymers and Surfactants at Fluid Interfaces Studied with Specular Neutron Reflectometry. *Adv. Colloid Interface Sci.* **2017**, *247*, 130–148. https://doi.org/10.1016/j.cis.2017.07.005.

(7) Skoda, M. W. A. Recent Developments in the Application of X-Ray and Neutron Reflectivity to Soft-Matter Systems. *Curr. Opin. Colloid Interface Sci.* **2019**, *42*, 41–54. https://doi.org/10.1016/J.COCIS.2019.03.003.

(8) Campbell, R. A.; Wacklin, H. P.; Sutton, I.; Cubitt, R.; Fragneto, G. FIGARO: The New Horizontal Neutron Reflectometer at the ILL. *Eur. Phys. J. Plus* **2011**, *126* (11), 1–22. https://doi.org/10.1140/epjp/i2011-11107-8.

(9) Gutfreund, P.; Saerbeck, T.; Gonzalez, M. A.; Pellegrini, E.; Laver, M.; Dewhurst, C.; Cubitt, R. Towards Generalized Data Reduction on a Chopper-Based Time-of-Flight Neutron Reflectometer. *J. Appl. Crystallogr.* **2018**, *51* (3), 606–615. https://doi.org/10.1107/S160057671800448X.

(10) Nelson, A. Co-Refinement of Multiple-Contrast Neutron / X-Ray Reflectivity Data Using MOTOFIT. *J. Appl. Crystallogr.* **2006**, *39*, 273–276. https://doi.org/10.1107/S0021889806005073.

(11) Campbell, R. A.; Tummino, A.; Noskov, B. A.; Varga, I. Polyelectrolyte/Surfactant Films Spread from Neutral Aggregates. *Soft Matter* **2016**, *12* (24), 5304–5312. https://doi.org/10.1039/c6sm00637j.

(12) Campbell, R. A.; Saaka, Y.; Shao, Y.; Gerelli, Y.; Cubitt, R.; Nazaruk, E.; Matyszewska, D.; Lawrence, M. J. Structure of Surfactant and Phospholipid Monolayers at the Air/Water Interface Modeled from Neutron Reflectivity Data. *J. Colloid Interface Sci.* **2018**, *531*, 98–108. https://doi.org/10.1016/j.jcis.2018.07.022.